

# High-speed optical frequency-domain imaging

S. H. Yun, G. J. Tearney, J. F. de Boer, N. Iftimia and B. E. Bouma

Harvard Medical School and Wellman Laboratories for Photomedicine,  
Massachusetts General Hospital  
50 Blossom Street, BAR-7, Boston, Massachusetts 02114  
[syun@bics.bwh.harvard.edu](mailto:syun@bics.bwh.harvard.edu)

**Abstract:** We demonstrate high-speed, high-sensitivity, high-resolution optical imaging based on optical frequency-domain interferometry using a rapidly-tuned wavelength-swept laser. We derive and show experimentally that frequency-domain ranging provides a superior signal-to-noise ratio compared with conventional time-domain ranging as used in optical coherence tomography. A high sensitivity of  $-110$  dB was obtained with a 6 mW source at an axial resolution of  $13.5$   $\mu\text{m}$  and an A-line rate of  $15.7$  kHz, representing more than an order-of-magnitude improvement compared with previous OCT and interferometric imaging methods.

©2003 Optical Society of America

**OCIS codes:** (110.4500) Optical coherence tomography; (140.3600) Lasers, tunable; (170.4500) Optical coherence tomography; (170.3880) Medical and biological imaging

---

## References and links

1. D. Huang, E. A. Swanson, C. P. Lin, J. S. Schuman, W. G. Stinson, W. Chang, M. R. Hee, T. Flotte, K. Gregory, C. A. Puliafito, and J. G. Fujimoto, "Optical coherence tomography," *Science* **254**, 1178-1181 (1991).
2. R. C. Youngquist, S. Carr, and D. E. N. Davies, "Optical coherence-domain reflectometry: A new optical evaluation technique," *Opt. Lett.*, **12**, 158-160 (1987).
3. K. Takada, I. Yokohama, K. Chida, and J. Noda, "New measurement system for fault location in optical waveguide devices based on an interferometric technique," *App. Opt.* **26**, 1603-1606 (1987).
4. B. E. Bouma and G. J. Tearney, *Handbook of optical coherence tomography* (Marcel Dekker, New York, 2002).
5. G. J. Tearney, M. E. Brezinski, B. E. Bouma, S. A. Boppart, C. Pitris, J. F. Southern, and J. G. Fujimoto, "In vivo endoscopic optical biopsy with optical coherence tomography," *Science* **276**, 2037-2039 (1997).
6. G. J. Tearney, B. E. Bouma, and J. G. Fujimoto, "High speed phase- and group-delay scanning with a grating based phase control delay line," *Opt. Lett.* **22**, 1811-1813 (1997).
7. M. Rollins, S. Yazdanfar, M. D. Kulkarni, R. Ung-Arunyawee, and J. A. Izatt, "In vivo video rate optical coherence tomography," *Opt. Express* **3**, 219-229 (1998), <http://www.opticsexpress.org/abstract.cfm?URI=OPEX-3-6-219>
8. J. M. Schmitt, "Optical coherence tomography (OCT): A review," *IEEE J. Sel. Top. Quantum Electron.* **5**, 1205-1215 (1999).
9. F. Fercher, C. K. Hitzenberger, G. Kamp, S. Y. El-Zaiat, "Measurement of intraocular distances by backscattering spectral interferometry," *Opt. Commun.* **117**, 443-448 (1995).
10. G. Hausler and M. W. Lindner, "Coherence Radar and Spectral Radar - new tools for dermatological diagnosis," *J. Biomed. Opt.* **3**, 21-31 (1998).
11. R. Leitgeb, C. K. Hitzenberger, and A. F. Fercher, "Performance of Fourier domain vs. time domain optical coherence tomography," *Opt. Express* **11**, 889-894 (2003), <http://www.opticsexpress.org/abstract.cfm?URI=OPEX-11-8-889>
12. J. F. de Boer, B. Cense, B. H. Park, M. C. Pierce, G. J. Tearney, and B. E. Bouma, "Improved signal-to-noise ratio in spectral-domain compared with time-domain optical coherence tomography," *Opt. Lett.* **28**, 2067-2069 (2003).
13. E. Brinkmeyer and R. Ulrich, "High-resolution OCDR in dispersive waveguide," *Electron. Lett.* **26**, 413-414 (1990).
14. S. R. Chinn, E. Swanson, J. G. Fujimoto, "Optical coherence tomography using a frequency-tunable optical source," *Opt. Lett.* **22**, 340-342 (1997).
15. B. Golubovic, B. E. Bouma, G. J. Tearney, and J. G. Fujimoto, "Optical frequency-domain reflectometry using rapid wavelength tuning of a Cr<sup>4+</sup>:forsterite laser," *Opt. Lett.* **22**, 1704-1706 (1997).

16. F. Lexer, C. K. Hitzenberger, A. F. Fercher, and M. Kulhavy, "Wavelength-tuning interferometry of intraocular distances," *Appl. Opt.* **36**, 6548-6553 (1997).
17. S. H. Yun, C. Boudoux, G. J. Tearney, and B. E. Bouma, "High-speed wavelength-swept semiconductor laser with a polygon-scanner-based wavelength filter," *Opt. Lett.* **28**, 1981-1983 (2003).
18. W. V. Sorin, "Optical reflectometry for component characterization" in *Fiber optic test and measurement*, D. Derickson, ed. (Hewlett Packard Company, Prentice Hall, New Jersey, 1998).
19. J. G. Proakis and D. G. Manolakis, *Digital signal processing: principles, algorithms, and applications* (Prentice-Hall, Inc., New Jersey, 1996).
20. M. A. Choma, M. V. Sarunic, C. Uang, and J. A. Izatt, "Sensitivity advantage of swept source and Fourier domain optical coherence tomography," *Opt. Express* **11**, 2183-2189 (2003), <http://www.opticsexpress.org/abstract.cfm?URI=OPEX-11-18-2183>
21. K. Takada, K. Yukimatsu, M. Kobayashi, and J. Noda, "Rayleigh backscattering measurement of single-mode fibers by low coherence optical time-domain reflectometer with 14  $\mu\text{m}$  spatial resolution," *Appl. Phys. Lett.* **59**, 143-145 (1991).
22. W. V. Sorin and D. M. Baney, "A simple intensity noise reduction technique for optical low-coherence reflectometry," *IEEE Photon. Technol. Lett.* **4**, 1404-1406 (1994).
23. G. J. Tearney, H. Yabushita, S. L. Houser, H. T. Aretz, I. K. Jang, K. Schlendorf, C. R. Kauffman, M. Shishkov, E. F. Halpern, and B. E. Bouma, "Quantification of macrophage content in atherosclerotic plaques by optical coherence tomography," *Circulation* **106**, 113-119 (2003).

## 1. Introduction

Optical coherence tomography (OCT) allows minimally-invasive cross-sectional imaging of biological samples [1] and has been investigated for numerous applications in biology and medicine. In most OCT systems, one-dimensional (depth) ranging is provided by low-coherence interferometry [2,3] in which the optical path length difference between the interferometer reference and sample arms is scanned linearly in time. This embodiment of OCT, referred to as 'time-domain OCT', has demonstrated promising results for early detection of disease [4-8]. The relatively slow imaging speed (approximately 2 kHz A-line rate) of time-domain OCT systems, however, has precluded its use for screening of large tissue volumes, which is required for a wide variety of medical applications. Imaging speed has a fundamental significance because of its relationship to detection sensitivity (minimum detectable reflectivity). As the A-line rate increases, the detection bandwidth should be increased proportionally, and therefore the sensitivity drops [4]. The sensitivity of state-of-the-art time-domain OCT systems operating at 2-kHz ranges between  $-105$  and  $-110$  dB. Most biomedical applications require this level of sensitivity for sufficient depth of penetration and cannot tolerate a reduction in sensitivity to achieve a higher frame rate. Although increasing the optical power would, in principle, improve the sensitivity, available sources and maximum permissible exposure levels of tissue represent significant practical limitations.

One potential solution to high-speed imaging is offered by spectral-domain OCT ('spectral radar') where individual spectral components of low coherence light are detected separately by use of a spectrometer and a charge-coupled device (CCD) array [9,10]. The fast readout speed of CCD arrays and the signal-to-noise (SNR) advantage of the spectral-domain OCT [11,12] make it promising for some high-speed and low-power applications. However, the use of CCD arrays may cause problems associated with phase washout by changes in the sample arm length during the pixel integration time [11].

In this paper, we demonstrate optical frequency-domain imaging (OFDI) based on optical frequency-domain reflectometry [13-16] using a wavelength tunable laser and standard photodetectors. We derive and show experimentally that optical frequency domain ranging provides a significant SNR gain over time-domain ranging. Our OFDI system utilizes a recently developed 6 mW wavelength-swept laser [17] to achieve a ranging depth of 3.8 mm, an A-line acquisition rate of 15.7 kHz, a free-space axial resolution of 13.5  $\mu\text{m}$ , and a high sensitivity of  $-110$  dB.

## 2. Principle

### 2.1 Optical frequency domain reflectometry (OFDR)

Fig 1 shows the basic configuration of OFDR using a tunable light source and a fiber-optic interferometer. The output of the source is split into a reference arm and a sample arm which illuminates and receives the light reflected from within the sample. The interference between the reference- and sample-arm light is detected with a square-law photodetector while the wavelength of the monochromatic source is swept and the path lengths of the reference and sample arm are held constant. The axial reflectivity profile (A-line) is obtained by discrete Fourier transform (DFT) of the sampled detector signals [13].

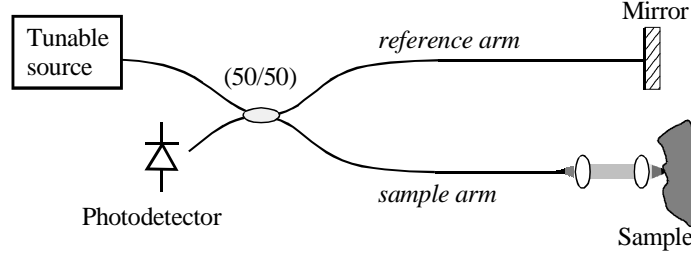


Fig. 1. Basic configuration of OFDR.

The detector current can be expressed as

$$i_{\text{det}}(t) = \frac{\eta q}{h\nu} \left( P_r + P_o \int r^2(z) dz + 2\sqrt{P_r P_o} \int r(z) \Gamma(z) \cos(2k(t)z + \phi(z)) dz \right), \quad (1)$$

where  $\eta$  is the detector sensitivity,  $q$  the quantum of electric charge ( $1.6 \times 10^{-19}$  coulomb),  $h\nu$  the single photon energy,  $P_r$  the optical power reflected from the reference arm at the photodetector,  $P_o$  the optical power illuminating to the sample. The third term represents the interferometric signal, and the first and second terms contribute to the non-interference background. Here,  $z$  is the axial coordinate where  $z=0$  corresponds to zero optical path length difference between the two interferometric arms,  $r(z)$  and  $\phi(z)$  are the amplitude and phase of the reflectance profile of the sample, respectively,  $\Gamma(z)$  is the coherence function of the instantaneous laser output, and  $k(t) = 2\pi/\lambda(t)$  is the wave number which is varied in time monotonically by tuning of the laser. It can be readily seen that the interferometric signal current is related to the reflection profile via the Fourier transform relation. In practice, the detector output is digitized and sampled into a finite number of data points, and a discrete Fourier transform (DFT) is performed to construct an axial scan or A-line.

For a tuning source with a Gaussian-profile spectral envelope, the axial resolution is given by [16]

$$\delta z = \frac{2 \ln 2}{\pi} \frac{\lambda_o^2}{n \Delta \lambda}, \quad (2)$$

where  $\lambda_o$  is the center wavelength,  $\Delta \lambda$  is the full-width-at-half-maximum (FWHM) of the spectral envelope (tuning range), and  $n$  is the group refractive index of the sample. The depth range  $\Delta z$  in the Fourier domain is given by [4,10]

$$\Delta z = \frac{\lambda_o^2}{4n \delta \lambda}, \quad (3)$$

where  $\delta \lambda = \Delta \lambda / N_s$  is the sampling wavelength interval and  $N_s$  is the number of samples within FWHM range of the spectrum  $\Delta \lambda$ . The sampling interval should be smaller than the instantaneous linewidth of the source; otherwise the amplitude of the coherence function will decay with  $z$ , limiting the usable ranging depth.

## 2.2 Signal and noise current

For simplicity, let us consider the case of a single reflector located at  $z=z_0$  with reflectivity  $r^2$ . We assume that the linewidth is sufficiently narrow so that  $\Gamma(z)=1$  within the depth range. The signal current,  $i_s(t)$ , can be expressed as

$$i_s(t) = \frac{\eta q}{h\nu} \cdot 2\sqrt{P_r P_s} \cos(2k(t) z_0), \quad (4)$$

where  $P_s=r^2P_0$  denotes the optical power reflected from the sample at the photodetector. In reality, the detector current consists of both signal and noise components such that  $i(t) = i_s(t) + i_n(t)$ . The well-known expression for the noise power  $\langle i_n^2 \rangle$  is given by [18]

$$\langle i_n^2(t) \rangle = \left( i_{th}^2 + 2 \frac{\eta q^2}{h\nu} (P_r + P_s) + \left( \frac{\eta q}{h\nu} \right)^2 RIN (P_r + P_s)^2 \right) BW, \quad (5)$$

where the three terms on the right hand side represent thermal noise, shot noise, and the relative intensity noise (RIN) of the source (polarized), respectively. Brackets  $\langle \rangle$  denote a time average,  $i_{th}$  the detector noise current,  $RIN$  the relative intensity noise given in unit of  $\text{Hz}^{-1}$ , and  $BW$  the detection bandwidth. The detection bandwidth can be chosen equal to half the sampling rate as specified by the Nyquist theorem [19].

## 2.3 Signal to Noise Ratio (SNR)

In the following, we will derive the signal to noise ratio in OFDR. For simplicity, let us assume a square-profile spectral envelope and 100% tuning duty cycle, i.e., the output power of the source is constant in time. Let  $F_s$  and  $F_n$  denote the Fourier transform samples of signal and noise currents,  $i_s$  and  $i_n$ , respectively, following DFT via

$$F(z_l) = \sum_{m=0}^{N_s-1} i(k_m) \cdot \exp^{-j2\pi l m / N_s} \quad (6)$$

Note that the wave number and axial coordinate are conjugates to each other through DFT. In the Fourier domain, the absolute square of the peak value of  $F_s$  at  $z_l = z_0$  is proportional to the reflectivity. Parseval's theorem,  $\sum F^2 = N_s \sum i^2$ , holds for both signal and noise [19]. In the case of Nyquist sampling (i.e. the sampling rate is equal to twice the detection bandwidth) the sampled data of noise current are mutually uncorrelated [11,12]. Therefore, the noise power level in the Fourier domain is given by  $\langle F_n^2 \rangle = N_s \langle i_n^2 \rangle$ . On the other hand, the signal power  $F_s^2$  is zero except at  $z_l = z_0$ . Since there are two peaks corresponding to positive and negative frequency components, using  $|F_s(z_0)|^2 = (N_s^2/2) \langle i_s^2 \rangle$  leads to

$$(SNR)_{FD} = \frac{|F_s(z_0)|^2}{\langle F_n^2 \rangle} = \frac{N_s}{2} (SNR)_{TD}, \quad (7)$$

where

$$(SNR)_{TD} = \frac{\langle i_s^2(t) \rangle}{\langle i_n^2(t) \rangle} \quad (8)$$

Here, the latter is defined as the ratio of the signal and noise power in the time-domain. These equations indicate that frequency-domain ranging provides an SNR improvement by a factor of  $N_s/2$  compared with time-domain ranging. A similar expression to Eq. (7) has been demonstrated by Leigeb *et al.* [11] and de Boer *et al.* [12] for spectral-domain OCT and also recently by Choma *et al.* [20] for OFDR using a swept source.

It can be shown that Eq. (7) is valid for a more general case where the tuning duty cycle is less than 100%, the source's spectral envelope has a Gaussian profile, and the sampling range spans beyond the FWHM of the source spectrum. In this case,  $N_s$  is the number of sampling points within the FWHM of the source and the optical powers,  $P_r$  and  $P_s$ , would be the time-

average value over one tuning cycle. For a shot noise limited system, Eqs. (5) and (7) with  $P_s \ll P_r$  lead to

$$(SNR)_{FD} \approx \frac{\eta P_s}{h\nu f_A}, \quad (9)$$

where  $f_A$  is the A-line rate which is the same as the tuning rate of the source. Therefore, the effective detection bandwidth in OFDR is equal to the A-line scan rate instead of the detector bandwidth.

Equation (7) can also be expressed in terms of the number of spatially resolvable points in a ranging depth,  $N_R = \Delta z / \delta z$ , as

$$(SNR)_{FD} = N_R (SNR)_{TD} \quad (10)$$

This expression compares the SNR of two ranging methods, time-domain and frequency-domain, at the same imaging speed (A-line rate), axial resolution, and ranging depth. Note that a time-domain OCT system requires a detection bandwidth of  $N_R f_A$ , whereas the effective noise bandwidth of OFDI is  $f_A$ .

The sensitivity is defined as the reflectivity that produces signal power equal to the noise power. Therefore, it follows from Eq. (9) and  $P_s = r^2 P_0$  that

$$\text{Sensitivity}[dB] = -10 \log \left( \frac{\eta P_0}{h\nu f_A} \right) \quad (11)$$

### 3. Experiment

#### 3.1 OFDI system configuration

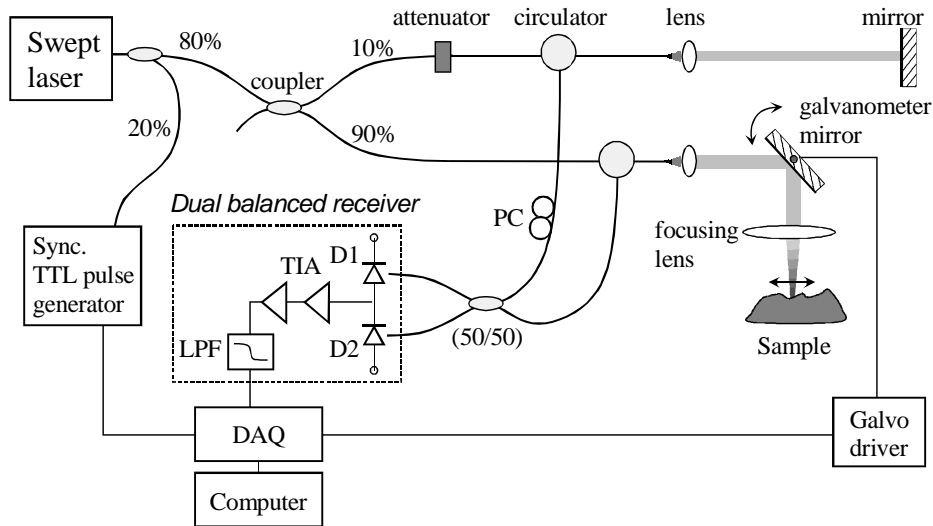


Fig. 2. Experimental configuration of the optical frequency domain imaging system.

Figure 2 shows the experimental configuration of the OFDI system. The optical source is an extended-cavity semiconductor wavelength-swept laser employing an intracavity polygon-scanner filter [17]. The laser was operated at a tuning rate of 15.7 kHz. Detailed operating principles and configuration of the laser are described in Ref. [17]. The laser generates cw polarized light at  $\lambda_0=1320$  nm with an average output power of 6 mW. The instantaneous linewidth of our laser was measured to be 0.06 nm (FWHM), corresponding to a span of 370 longitudinal modes (mode spacing: 28 MHz). To generate a synchronization signal, 20% of the laser output is tapped and detected with a fast InGaAs photodetector through a

narrowband fixed-wavelength filter. The detector generates a pulse when the output spectrum of the laser sweeps through the narrow passband of the filter. The detector pulse is fed to a digital circuit for conversion to a TTL pulse train. The TTL pulses were used to generate gating pulses for signal sampling. 90% of the remaining light is directed to the sample arm and 10% to the reference mirror. The light in the sample arm illuminates a sample through an imaging lens with a confocal parameter of 1.14 mm (twice the Rayleigh range in air) and transverse resolution ( $1/e^2$  spot diameter) of 30  $\mu\text{m}$  (in air). A galvanometer-mounted mirror scans the probe light transversely on the sample over 5 mm at 30 Hz. The total optical power illuminated on the sample was approximately 3.5 mW. The light reflected from the reference mirror and the sample were received through magneto-optic circulators and combined by a 50/50 coupler. A fiber-optic polarization controller (PC) in the reference arm was used to align the polarization states of the two arms.

The relative intensity noise (RIN) of polarized thermal light is proportional to the reciprocal of the linewidth [18] and would have a value of  $-97$  dB/Hz for a linewidth of 0.06 nm (10 GHz). In general, RIN of laser light is different from that of thermal light. However, laser light consisting of many longitudinal modes with random phases would exhibit a peak RIN level similar to that of thermal light of the same linewidth. Mode hopping associated with wavelength tuning and gain competition contributes to the frequency dependence of RIN. The RIN level of our laser had a peak value of approximately  $-100$  dB/Hz near DC frequency, decreasing to  $-120$  dB/Hz at 5 MHz. To reduce the source's RIN, dual balanced detection was employed [21]. The differential current of two InGaAs detectors D1 and D2 was amplified using trans-impedance amplifiers (TIA, total gain of 56 dB) and passed through a low pass filter (LPF) with a 3-dB cutoff frequency at 5 MHz and excess voltage loss of 3 dB. The common-noise rejection efficiency of the receiver was approximately 25 dB in the range between DC and 5 MHz. In addition to RIN reduction, the balanced detection provides multiple benefits; it suppresses self-interference noise [11] originating from multiple reflections within the sample and optical components; it also improves the dynamic range and reduces fixed-pattern noise by greatly reducing the strong background signal from the reference light.

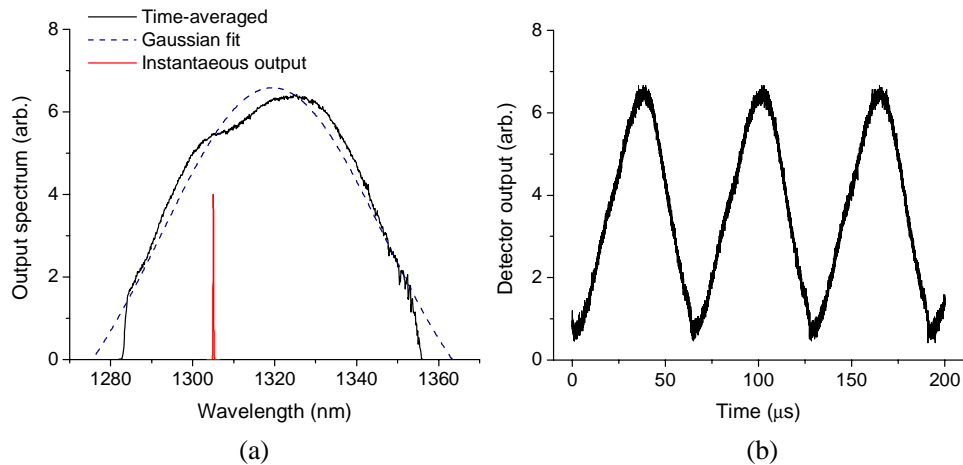


Fig. 3. (a) Integrated output spectrum (solid, black) of the wavelength-swept laser operating at a sweep rate of 15.7 kHz, Gaussian fit of the integrated spectrum (dashed, black), and instantaneous spectrum (solid, red). (b) Laser intensity output as a function of time (three cycles).

Figure 3(a) shows the time-averaged output spectrum, measured at the output port of the laser with an optical spectrum analyzer in peak-hold mode (resolution bandwidth = 0.07 nm).

The total tuning range was 74 nm, determined by the free spectral range of the polygon-scanner filter. The spectral envelope has a Gaussian-like profile. A best-fit Gaussian curve is presented in Fig. 3(a), with FWHM  $\Delta\lambda=63.5$  nm. Eq. (2) predicts an axial resolution of 12.1  $\mu\text{m}$  (in air). Fig. 3(a) also shows an output spectrum (solid red), measured while the intracavity filter was fixed to a particular wavelength. The narrow linewidth contrasts with the time-averaged broad spectral envelope. The instantaneous linewidth (0.06 nm) of the laser was determined from its measured double-pass coherence length of 6.4 mm (FWHM). A ranging depth of 6.4 mm offered by the narrow instantaneous linewidth is superior to that achieved by other clinical OCT systems and enables imaging of tissues with large surface height variations. Fig. 3(b) is the oscilloscope trace of the laser output detected with a photodetector (bandwidth 5 MHz) at the laser output port.

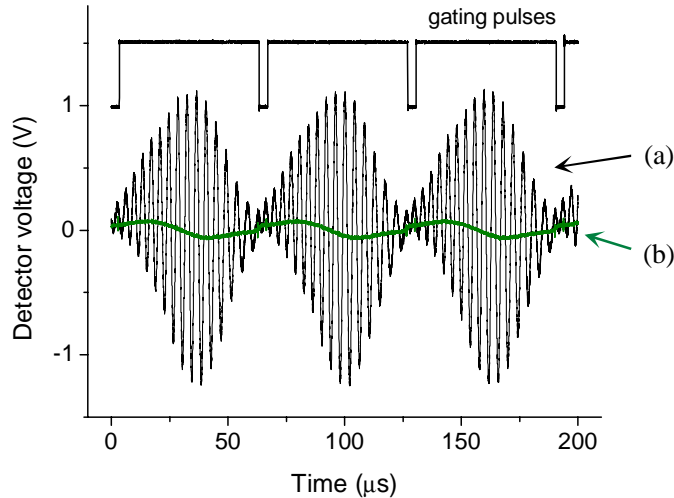


Fig. 4. (a) Interference signal for a weak reflector sample measured with dual balanced receiver, (b) background component measured by blocking the sample arm. The upper trace is the gating pulse train used for the data acquisition.

Figure 4(a) shows an exemplary output of the balanced receiver when a partial reflector was placed at the focus of the imaging lens in the sample arm. The reference mirror was placed such that the optical path length difference between the two interferometer arms was 200  $\mu\text{m}$ . Fig. 4(b) is the background detector voltage when the sample arm was blocked. The residual background signal from the reference light is due to the wavelength-dependent splitting ratio of the 50/50 coupler. This background signal can contribute to image noise and was minimized through digital subtraction prior to DFT. The receiver output was digitized using a data acquisition board (DAQ) with 12-bit resolution and acquired at a sampling speed of 10 Ms/s. The upper trace in Fig. 4 is the gating pulse train generated from the DAQ board triggered by the TTL sync pulses. During the high state of the gating pulse, a total of 600 data points were obtained on each wavelength sweep. We note that the acquisition rate limited the sampling frequency resulting in a ranging depth of 3.8 mm instead of 6.4 mm. The duty cycle of the sampling was 94%. Data processing of each A-line involves an interpolation and mapping from wavelength- to k-space process prior to DFT [13]. This step was critical to obtain transform-limited axial resolution and optimal sensitivity performance. 300 pixels per A-line were obtained from a DFT of 600 points. The galvanometer controlling the transverse location of the ranging beam on the sample was driven with a saw-tooth waveform at 30 Hz to produce 520 A-lines per image.

### 3.2 SNR and Sensitivity

To determine the optimum reference arm power for maximum sensitivity, the SNR was measured as a function of the reference arm power for a partial reflector sample. The sample comprised neutral-density filters (−55 dB) and a metal mirror and was positioned at the focal plane of the sample arm. From the measured SNR value, the sensitivity of the system was determined. Fig. 5(a) is the experimental result measured as a function of the reference-arm power at the photodiode. The reference arm power was changed from 0.1 to 80  $\mu\text{W}$  using a variable neutral-density filter placed in front of the reference mirror (not shown in Fig. 2). The position of the reference mirror was adjusted to have the signal peak in the middle of the ranging window, i.e.  $z = 1.92$  mm. The results show that the reference power of 10-20  $\mu\text{W}$  produces the best sensitivity of about −110 dB.

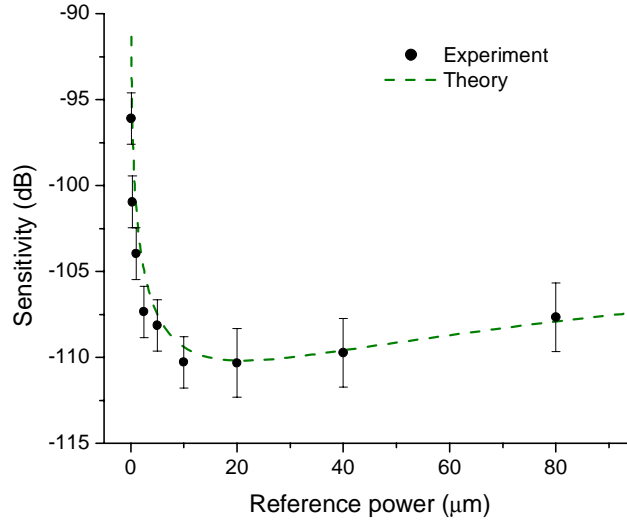


Fig. 5. Sensitivity measured as a function of the reference-arm optical power (black dots) and the theoretical curve (green dashed line).

In the case of dual balanced detection, the signal power in Eq. (4) can be expressed as

$$\langle i_s^2(t) \rangle = \left( \frac{\eta q}{h\nu} \right)^2 \left\langle \sum^2 2p_r p_s \cos(kz) \right\rangle^2 = 8 \left( \frac{\eta q}{h\nu} \right)^2 p_r p_s, \quad (12)$$

where  $p_r = P_r/2$  and  $p_s = P_s/2$  denote the reference and signal power per photodiode. The noise power expression in Eq. (5) can be modified to

$$\langle i_n^2(t) \rangle = \left( \frac{i_{qn}^2}{G^2} + \frac{i_{ex}^2}{G^2} + i_{th}^2 + 2 \frac{\eta q^2}{h\nu} \sum^2 (p_r + p_s) + \left( \frac{\eta q}{h\nu} \right)^2 RIN \left\{ \sum^2 \zeta (p_r^2 + p_s^2) + \sum^2 2p_r p_s \right\} \right) BW \quad (13)$$

Here, the first and second terms are introduced to take into account the quantization noise and excess electrical noise generated in the DAQ board.  $G$  denotes the total gain of the receiver. The third term is the thermal noise of the dual balanced receiver. The fourth term represents the total shot noise which is a sum of the shot noise from the individual photodiodes. The fifth term expresses the RIN noise with  $\zeta$  denoting the common-mode rejection efficiency of the balanced receiver. It should be noted that the dual balanced receiver provides RIN suppression only to the RIN component associated with intraband self beating. The cross beating noise, as a result of the incoherent interference between  $p_r$  and  $p_s$ , is not canceled. When  $\zeta \ll 1$ , the cross-beating RIN component may not be negligible compared to the self-beating RIN component although  $p_s$  is weaker than  $p_r$ . In our system, the first two terms, quantization and

excess noise, were made negligible by choosing a sufficiently high gain of  $G = 2 \times 10^5$ . Fig. 5 shows the theoretical curve calculated from Eqs. (12), (13), and (7) compared with the experimental values. In this calculation, we used experimentally measured parameters:  $p_s = 3.8 \text{ nW}$ ,  $i_{th} = 6 \text{ pA}/\sqrt{\text{Hz}}$ ,  $\eta = 1$ ,  $RIN = 1 \times 10^{-11}/\text{Hz}$  ( $-110 \text{ dB/Hz}$ ),  $\zeta = 3.16 \times 10^{-3}$  ( $-25 \text{ dB}$ ),  $BW = 5 \times 10^6 \text{ Hz}$ , and  $N_s/2 = 260$ . The theory is in good agreement with the experimental result.

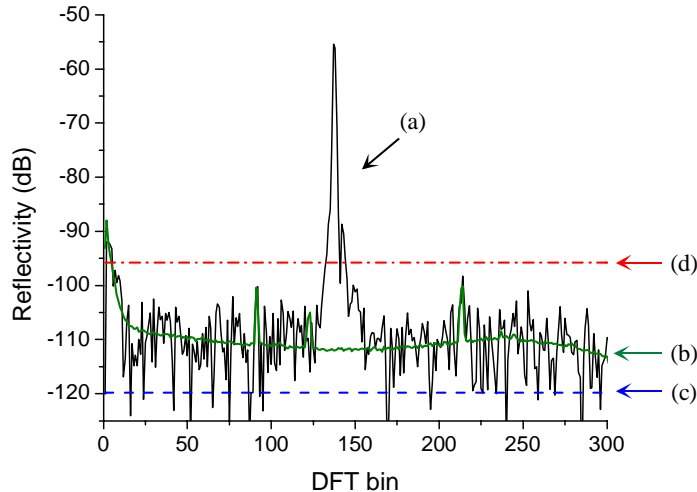


Fig. 6. Sensitivity measured (a, black solid line) with a  $-55 \text{ dB}$  partial reflector, (b, green solid line) with the sample arm blocked. (c, blue dashed line) and (d, red dash-dot line) are theoretical maximum sensitivity of hypothetical shot-noise limited frequency-domain and time-domain OCT with a detection bandwidth of  $5 \text{ MHz}$ .

Figure 6 depicts our OFDI A-line profile from a partial reflector ( $-55 \text{ dB}$ ) placed (curve a). The reference arm power was adjusted to be  $15 \text{ }\mu\text{W}$  per photodetector for maximum sensitivity by using an optical attenuator [22]. The sample-arm optical power at the receiver was  $3.8 \text{ nW}$  per photodetector. The x-axis represents the 300 DFT components corresponding to the frequency from DC to  $5 \text{ MHz}$  and a total ranging depth of  $3.85 \text{ mm}$  (in air). The measured ranging depth determines, from Eq. (3), the sampling interval  $\delta\lambda = 0.113 \text{ nm}$  which agrees well with the estimated value of  $0.116 \text{ nm}$  assuming a linear tuning slope. From the measured SNR of  $55 \text{ dB}$ , the sensitivity of the system is determined to be  $-110 \text{ dB}$ . Curve (b) is the noise level measured without the partial reflector, averaged over 520 consecutive A-lines, demonstrating that our OFDI system is capable of detecting signals with a high dynamic range of  $>55 \text{ dB}$ . Curve (c) is the theoretical limit of sensitivity calculated from Eq. (11). The experimental sensitivity was approximately  $10 \text{ dB}$  lower than the ideal value. The difference is attributed to the detector thermal noise and incomplete cancellation of source RIN, both of which were dominant over the shot noise at the operating conditions. Dual balanced detection with a lower thermal noise and better RIN suppression will lead to several-dB of improvement in the system sensitivity. Further SNR improvement may be possible by shifting the detection frequency range, using an acousto- or electro-optic modulator, to higher frequencies where RIN of the laser is relatively smaller ( $<-125 \text{ dB/Hz}$ ). Curve (d) is the theoretical limit of a hypothetical time-domain system of the same speed, optical power, ranging depth, and detection bandwidth. We note, however, that a time domain system capable of scanning over  $\sim 4 \text{ mm}$  at an A-line rate of  $15.7 \text{ kHz}$  has not been demonstrated; the previous time domain speed record of Rollins et al. utilized a resonant galvanometer in a scanning delay line to achieve an A-line rate of  $4 \text{ kHz}$  [7]. Compared to the hypothetical time-domain system, our prototype system demonstrated an improvement in sensitivity of  $15 \text{ dB}$  and compared with the results of Rollins et al., the improvement of our OFDI system was approximately  $20 \text{ dB}$ . The same measurements were repeated at different optical delay lengths by varying the position of

the reference mirror in the reference arm. The measured sensitivity was  $-110 \pm 3$  dB in the entire depth range except for in the vicinity of DC and Nyquist frequency (5 MHz). The axial resolution was determined from Gaussian fits of the measured point spread functions and was  $13.5 \pm 1$   $\mu\text{m}$  throughout the entire depth range.

### 3.3 Images

Figure 7(a) depicts the ventral portion of a volunteer's finger acquired at 30 frames per second (fps). The image comprised of 300 axial x 520 transverse pixels plotted in logarithmic inverse grayscale. The focal point of the imaging lens was positioned in the middle of the depth range. The residual background signal, obtained by blocking the signal-arm power prior to image acquisition, was subtracted from the interference signal to reduce the fixed pattern noise [10,11]. However, some residual fixed pattern noise appears as horizontal lines in the image. For comparison to a time-domain OCT image, Fig. 7(b) shows the image of the same sample obtained with a state-of-the-art time-domain OCT system in our laboratory [23]. The OCT system uses a broadband amplified spontaneous emission source with 20 mW output power at a center wavelength of 1310 nm. The system was operated at 4 fps with a ranging depth of 2.5 mm, axial resolution of 10  $\mu\text{m}$ , transverse resolution of 20  $\mu\text{m}$ , and shot-noise-limited detection sensitivity of approximately  $-110$  dB. The OFDI image exhibits penetration as deep as the time-domain OCT image, despite the 8-fold faster imaging speed, 1.5-fold larger depth range, and 3-fold lower source power.

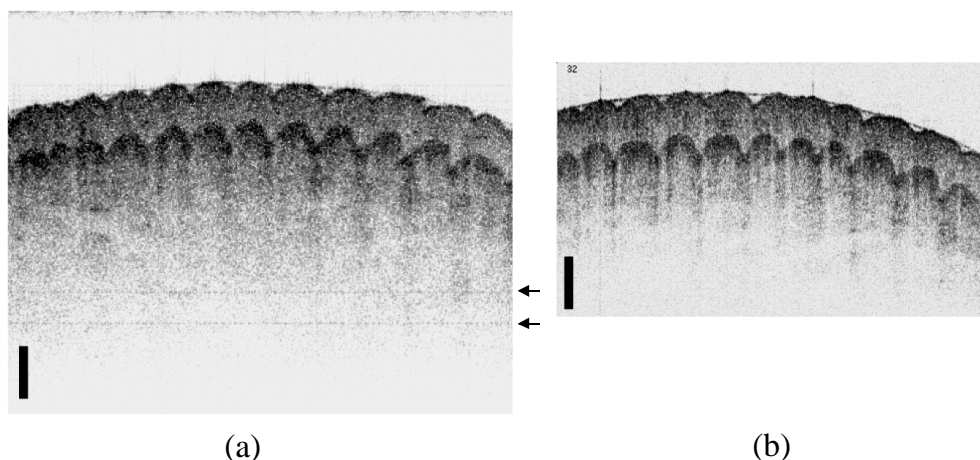


Fig. 7. (a) Image of a human finger (300 axial x 520 transverse pixels) acquired in vivo with the OFDI system at 30 fps. The vertical axis of this image contains 300 pixels and extends over a depth of 3.8 mm, where the horizontal axis of this image contains 520 pixels and extends over a transverse distance of 5.0 mm. (b) OCT image of the same human finger (250 axial x 500 transverse pixels, 2.5 x 5.0 mm) acquired at 4 fps using a state-of-the-art time-domain OCT system with a sensitivity of  $-110$  dB. Despite of the 8 times faster imaging speed and lower source power, the OFDI image exhibits as large a penetration depth as the time-domain image. The scale bar represents 0.5 mm. Arrows in (a) mark axial locations of residual fixed pattern noise.

## 4. Conclusion

We have demonstrated an optical frequency-domain imaging (OFDI) with 8 times faster imaging speed (A-line rate of 15.6 kHz) than the state-of-the-art time-domain OCT while maintaining a high sensitivity of  $-110$  dB. The SNR advantage of frequency-domain imaging over time-domain OCT should be critical to obtain clinically-meaningful sensitivity at high imaging speeds of greater than 10 kHz A-line rate. OFDI offers a simple way of implementing polarization diversity and, compared to spectral domain OCT, does not suffer from phase

washout due to sample arm motion during pixel integration time. We believe that OFDI has significant potential in biomedical imaging applications where high speed and high sensitivity are critical.

### **Acknowledgments**

This research was supported in part by the National Science Foundation (BES-0086709), Center for Integration of Medicine and Innovative Technology (CIMIT), and by a generous gift from Dr. and Mrs. J. S. Chen to the optical diagnostics program of the Massachusetts General Hospital Wellman Laboratories of Photomedicine.